Numerical investigations on the effect of an underbody battery on solar vehicle aerodynamics

JAKUB BOBROWSKI[*]
KRZYSZTOF SOBCZAK

Institute of Turbomachinery, Lodz University of Technology, 217/221 Wolczanska, 93-005 Łódź Poland

Abstract The placement of the battery box can have a massive impact on the aerodynamics of an electric vehicle. Although favourable from the viewpoint of vehicle dynamics, an underbody battery box may impair the vehicle aerodynamics. This study aims to quantify the effect of an underbody battery box on the drag force acting on an electric vehicle. Four different variants of the vehicle (original variant, lifted suspension, lifted suspension with an underbody battery box) are investigated by means of computational fluid dynamics. The underbody battery box was found to induce flow separation, resulting in a massive increase in drag force. As a solution, a battery box fairing was designed and tested. The fairing significantly reduced the increase in drag. The results of this study could contribute to the design of more stable and aerodynamically efficient electric vehicles.

Keywords: Automotive aerodynamics; Drag reduction; Electric vehicle; CFD, Underbody fairing

1 Introduction

In the context of rising energy prices, automobile manufacturers are seeking ways to render their vehicles more energy efficient. One way of achieving this is to reduce aerodynamic drag, which accounts for up to 50% of all energy losses experienced by an electric passenger vehicle [1]. It is a well-known fact that most drag on a passenger vehicle is generated at the rear

---
[*]Corresponding Author. Email: 223903@edu.p.lodz.pl

end [2,3], which must be carefully designed to produce low drag vehicles [4]. However, the performance of rear-end features (e.g. the diffuser) is strongly impacted by the upstream geometry, such as underbody details.

Buchheim *et al.* [4] reported that aerodynamic drag on the Volkswagen Research Car 2000 could be reduced by adjusting the diffuser angle, although the relation is quite complex. A significant decrease in drag was also achieved by lengthening the diffuser. In [5], the authors studied the aerodynamics of a generic automobile model. The downforce was observed to increase with larger diffuser angles. The same conclusion was reached in [6]. This relation has been established in the literature [7–9]. Potthoff reported that any deviation from the optimal diffuser angle of the Unicar research vehicle incurred a drag penalty [6]. While the diffuser angle has a fairly straightforward influence on the aerodynamic downforce, its effect on the drag force is ambiguous and dependent on the overall vehicle geometry.

There have also been numerous studies on the influence of underbody geometry on vehicle aerodynamics. In [10], the authors used the SST turbulence model to compute the flow field around twelve versions of the DrivAer model [11]. In [12], the authors employed a novel turbulence modelling approach called V-LES (very-large eddy simulation) [13] to simulate the flow field around four variants of the DrivAer notchback model. The results of these studies match the experimental data provided in [14,15]. They show that a vehicle with a detailed underbody generates more drag compared to one with a smooth underbody.

In addition to investigations into the impact of underbody details, numerous studies have focused on the effect of ground clearance (ride height) on vehicle aerodynamics. Janssen and Hucho examined several vehicles and concluded that there is no universal relation between drag force and ground clearance, although many vehicles with smaller ground clearance exhibit reduced drag [16]. In [5], the authors observed that the downforce increased with decreasing ground clearance, until a minimum was reached. This tendency has been confirmed in [7–9,17].

Here, we quantify the effect of ride height and an underbody battery box on electric vehicle aerodynamics. To the best knowledge of the authors, there have been no previous studies on the effect of an underbody battery box on electric vehicle aerodynamics. The analysis is based on a real road vehicle built by the Lodz Solar Team from Lodz University of Technology in Poland. Eagle Two (Fig. 1) is an electric vehicle powered by both solar panels and traditional electric batteries. When the regulations of the Bridgestone World Solar Challenge changed, the team was required

to install batteries with higher capacity, which were considerably larger and heavier than the previous compact batteries. To optimise the position of the centre of gravity, the battery box was placed underneath the vehicle. Since the minimum ground clearance required is 10 cm, we were forced to lift the suspension. A battery box fairing was also designed and tested, which greatly decreased the drag penalty caused by the underbody battery box. The design of the fairing is rather uncomplicated: it involves two planar surfaces at the upstream and downstream side of the battery box. This configuration aims to weaken the high-pressure region upstream from the battery box and prevent flow separation downstream from the battery box. While more complicated designs could exhibit better performance, this design provides a workable and cost-efficient solution for the Lodz Solar Team.

Figure 1: Eagle Two solar vehicle [18].

Four variants of the solar vehicle are analysed:

1) variant 1 – original ride height of 12 cm (Fig. 2),

2) variant 2 – lifted to a ride height of 22 cm (Fig. 3),

3) variant 2 with an underbody battery box (Fig. 4),

4) variant 3 with a battery box fairing (Fig. 5).

To reduce computational costs, the computer-aided design (CAD) models do not include the exact topology of the wheels and the suspension. These details would in any case have little effect on integral results (e.g. drag and lift force) [14, 15].
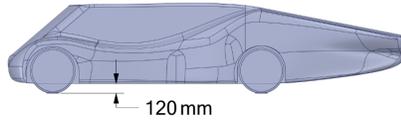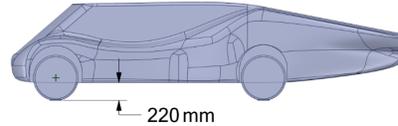
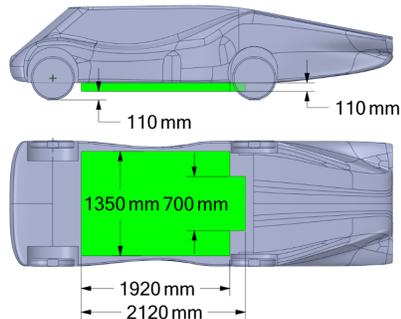Figure 2: Eagle Two variant 2.

Figure 3: Eagle Two variant 3.
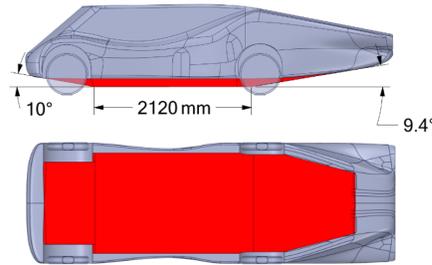

Figure 4: Eagle Two variant 4.

Figure 5: Eagle Two variant 5.

2   Methods

This section describes the computational fluid dynamics model that was used to compute the flow field around each variant of the solar vehicle. The model was prepared in the commercial package Ansys. The task was solved using the Ansys Fluent solver.

Enough space was allowed around the vehicle to avoid interference between the flow pattern and the farfield boundary conditions. The vehicle is approximately 5 m in length, 2 m in width, and 1 m in height. The dimensions of the computational domain are shown in Fig. 6. The domain has a blockage ratio of 0.7%, which is acceptably low [19]. Since the vehicle, the boundary conditions, and the flow field are symmetric, we exploited the symmetry condition and modelled one half of the domain.

The mesh was generated in Fluent Meshing. We chose the poly-hexcore architecture, which fills the bulk region with octree hexahedra, maintains a poly-prism inflation layer and conformally connects these two regions with general polyhedral volumes (Fig. 7). The poly-hexcore grid offers better overall quality than the traditional hexcore, while reducing the element count by about 40% [20]. The mesh in the proximity around and behind the vehicle was refined in order to properly capture the flow field. The surface mesh on the vehicle was refined based on wall curvature.
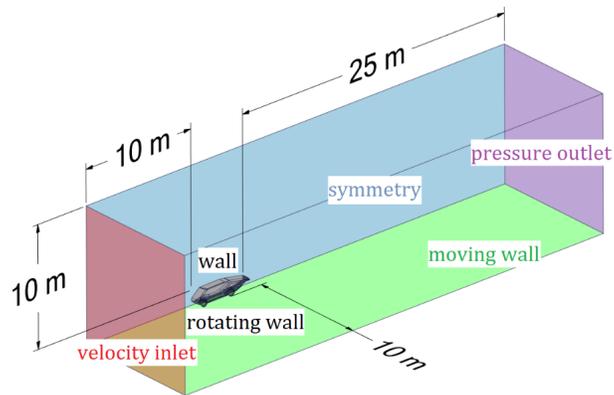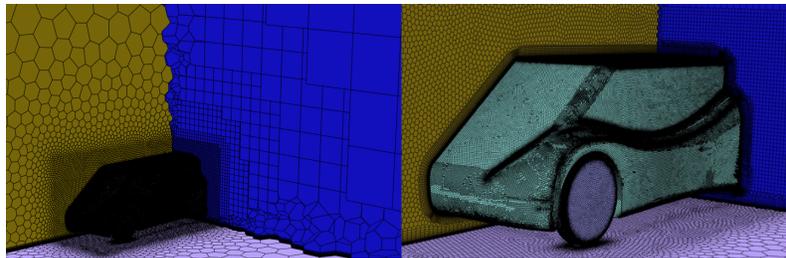
Figure 6: Enclosure around the vehicle.

Figure 7: Poly-hexcore mesh around the vehicle.

Inflation was created near the walls, thanks to which wall-normal gradients were accurately resolved. In this study, evaluation of the skin friction drag and accurate prediction of any flow separation are of key importance. Therefore, the Near Wall Model approach was adopted. This approach requires a high resolution near-wall mesh, which involves creating a sufficient number of sufficiently thin elements [21]. The thickness of the first layer and the boundary layer thickness were calculated from the flat plate boundary layer theory [22]. The resulting first layer thickness of $y = 0.02$ mm ensures that the dimensionless wall distance $y^+ < 1$ on almost the whole surface area of the vehicle walls. The number of layers was set to 37, thanks to which the inflation covered and extended beyond the entire boundary layer, in order not to restrict its growth.

The simulation represents the solar car travelling through air at a cruising speed of 22.2 m/s, which corresponds to the freestream Mach number $Ma_\infty = 0.07$. This value falls within the low-subsonic regime; com-

pressibility effects are therefore negligible. The density of air was set to $\rho = 1.225 \text{ kg/m}^3$, while the dynamic viscosity was set to $\mu = 1.789 \times 10^{-5} \text{ kg/(m} \cdot \text{s)}$.

To simulate this case, the steady-state Reynolds-averaged Navier–Stokes (RANS) approach was adopted. This provides a reasonable trade-off between accuracy and computational expense. RANS modelling is widely used in the automotive industry and has proven to be quite successful at predicting integral quantities, such as drag force [10, 19, 23–25]. Several papers indicate that scale-resolving models (e.g. detached eddy simulation) offer advantages over the traditional RANS approach [26, 27]. However, these models require substantially more computational power compared to the traditional RANS approach.

We employed the shear stress transport (SST) turbulence model to close the RANS equations [28]. This model is based on the Boussinesq concept of an isotropic eddy viscosity. This assumption typically works well for shear flows dominated by only one of the turbulent shear stresses [29], as is the case in our study. The SST formulation takes advantage of the two most popular turbulence models. The use of the low-Re k-omega formulation near the wall enables full boundary layer resolution and accurate prediction of flow separation. SST switches to the k-epsilon formulation in the bulk flow and thereby avoids the common problem that k-omega is overly sensitive to inlet turbulence properties. SST is more accurate and reliable for a wide class of flows, involving adverse pressure gradients and separation regions [28–31]. The SST turbulence model has been validated in numerous studies on automotive aerodynamics [10, 23–25]. In a NASA Technical Memorandum, SST was rated the most accurate model for aerodynamic applications [32]. All the model constants were left unchanged. Additionally, the Production Limiter was enabled to avoid excessive buildup of turbulence in the stagnation region, in accordance with [28].

The boundary conditions (shown in Fig. 6) were set up in accordance with the Fluent guidelines [19]. The boundary conditions represent the solar vehicle travelling at 22.2 m/s through still air. The relative motion of the ground with respect to the vehicle was taken into account, in order to properly capture the automotive ground effect. The rotating wheels were also modelled. The rotating wheels generate a significant amount of turbulence, which is convected downstream and affects the performance of the diffuser. The freestream turbulence properties were determined in accordance with the literature [33]. The inlet turbulence length scale was assumed to be equal to 40% of the maximum boundary layer thickness. The inlet tur-

bulence intensity was set to a value corresponding to steady atmospheric conditions. Details of the boundary conditions are presented in Table 1.

Table 1: Boundary conditions.

Location	Boundary condition type	Details
Upstream	Velocity inlet	Inlet velocity 22.2 m/s Turbulence intensity 1% Turbulence length scale 0.03 m
Downstream	Pressure outlet	Gauge static pressure 0 Pa
Vehicle body	No-slip wall	Smooth wall
Ground	No-slip moving wall	Velocity (downstream) 22.2 m/s, smooth wall
Front and rear wheels	No-slip rotating wall	Rotational velocity 79.4 rad/s, smooth wall
Elsewhere	Symmetry	–

A pressure-based coupled solver was used. Since the flow field was expected to be mildly unsteady, Pseudo-Transient under-relaxation was enabled. The pressure interpolation scheme was set to Standard. Spatial discretisation of momentum and turbulence properties were set to Second Order Upwind. Gradient reconstruction was set to Least Squares Cell Based. These settings are in accordance with the Ansys Fluent guidelines [21].

In order to judge iterative convergence, we monitored the residuals, the drag and lift force, and the wall shear stress contour (as an additional measure, to visualise separation regions). A sufficient number of iterations were executed to ensure that the solution had indeed achieved convergence. The solution was very slightly unsteady (the drag force monitor oscillated with an amplitude of about 1%). However, the residuals achieved good convergence. The solution was thus considered to be converged.

Once a stable solution had been reached, a grid convergence study was conducted to determine the optimal grid sizing and consequently establish a grid-independent solution. The simulation of variant 1 was performed on three grids of different resolution. Despite the grids being semistructured, grid refinement was performed in a structured manner (the inflation was not modified). We used a grid refinement ratio of 1.2 (each grid sizing except the inflation sizing was divided by 1.2), to allow the spatial discretisation error to be differentiated from other error sources (iterative convergence, grid distortion, etc.).

From Table 2 it can be observed that the drag force converges to a constant value. The difference between the results obtained on consecutive grids decreases. In subsequent simulations, the grid settings from the medium grid were adopted. The solution obtained on the medium grid is not fully mesh independent. Nonetheless, the medium grid offers sufficient precision at a reasonable computational expense.

Table 2: Poly-hexcore mesh around the vehicle.

Grid size	Drag force (N)
Coarse – 9.77×10^6	85.2
Medium – 13.4×10^6	89.1
Fine – 17.0×10^6	91.4

3   Results and discussion

The numeral results are shown in Table 3, including the aerodynamic forces and the respective dimensionless coefficients. Variant 1 is exceptionally streamlined, achieving a drag coefficient $C_D = 0.18$ (modern production sedans typically achieve a value of about 0.25–0.30). The lifted suspension of variant 2 weakens the automotive ground effect, generating 53% less downforce $-F_L$ compared to variant 1. This tendency is well established in the literature [7–9, 17]. In both variant 1 and variant 2, the downforce is dominated by the rear component, $-F_{RL}$. The diffuser is thus efficient at generating rear downforce. Variant 2 generates 10% more drag, F_D, compared to variant 1, although this difference is not pronounced.

Table 3: Aerodynamic forces and coefficients.

Variant	F_D (N)	C_D (–)	$-F_L$ (N)	$-C_L$ (–)	$-F_{FL}$ (N)	$-C_{FL}$ (–)	$-F_{RL}$ (N)	$-C_{RL}$ (–)
1	89	0.18	110	0.210	19	0.037	87	0.170
2	98	0.19	50	0.099	14	0.027	36	0.072
3	190	0.35	−120	−0.220	−87	−0.16	−30	−0.060
4	150	0.28	−29	−0.053	74	0.14	−100	−0.190

F_D – drag force, C_D – drag coefficient, F_L – lift force,
C_L – lift coefficient, F_{FL} – front lift force, C_{FL} – front lift coefficient,
F_{RL} – rear lift force, C_{RL} – rear lift coefficient.

In contrast to variants 1 and 2, which generate downforce, variant 3 generates significant lift, F_L. The lift force generated by this variant is dominated by the front lift, F_{FL}. Moreover, variant 3 experiences 93% more drag compared to variant 2. These are due to the high-pressure region upstream from the battery box and the boundary layer separation downstream from the battery box.

Thanks to the battery box fairing proposed in variant 4, the flow is now mostly attached. The drag penalty caused by the underbody battery box is reduced by 43%. The unwanted lift experienced by variant 3 is decreased by 75%.

Figure 8 shows the velocity field at the symmetry plane. In variants 1 and 2, the flow on this plane is attached. In variant 3, the fluid upstream from the battery box decelerates. This increases the pressure, which contributes to increased drag. A separation zone is visible downstream from the battery box, which further increases drag. Thanks to the battery box fairing in variant 4, the flow is attached in the central part of the vehicle.
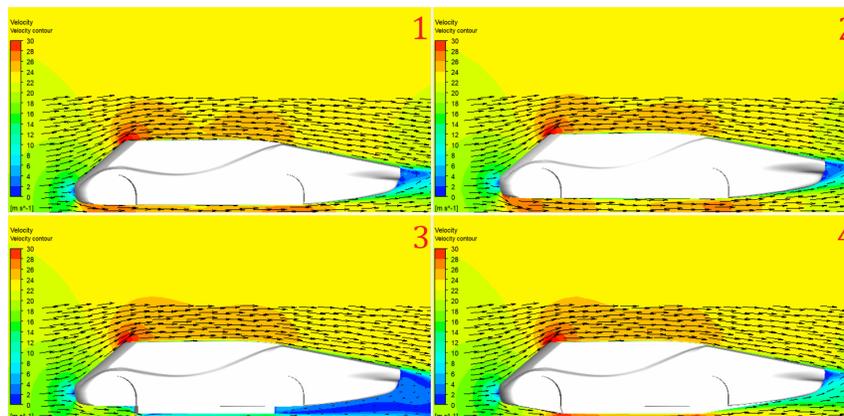

Figure 8: Velocity field at the symmetry plane.

Figure 9 shows a comparison of the velocity fields at the rear ends of each variant. The velocity vectors and contours are displayed on the symmetry plane and on two planes normal to the car motion located at distances of 0.6 m and 1.4 m from the rear axle. The flow around variant 1 is mostly attached, although there is a small separation zone behind the rear wheel. This separation zone is more pronounced in variant 2, since the wheels of variant 2 are more exposed. A massive flow separation can be observed behind the battery box in variant 3. Moreover, the presence of the battery

box magnifies the flow separation behind the rear wheel. These separations contribute to increased drag. The battery box fairing in variant 4 manages to prevent boundary layer separation in the central part of the diffuser. Nonetheless, the recirculation zone behind the rear wheel is considerably larger than in the previous variants. Therefore, the drag penalty is not reduced entirely.
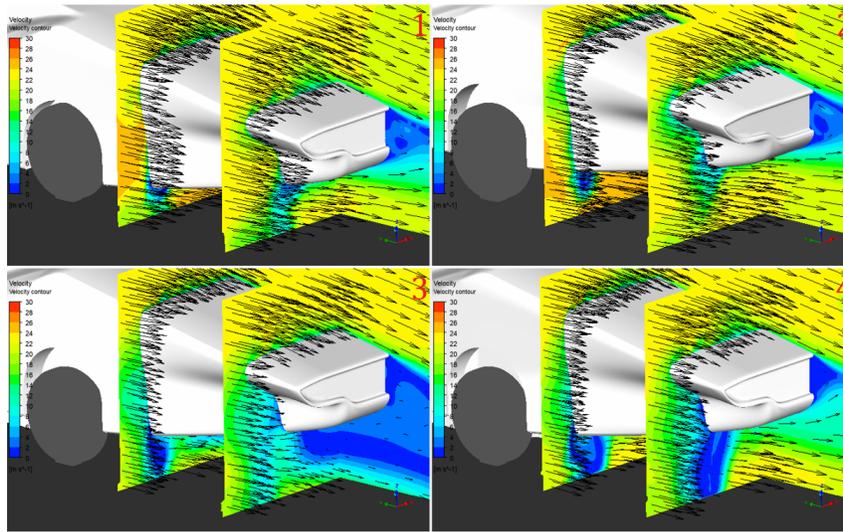

Figure 9: Velocity field towards the rear of the vehicles.

The pressure distribution on the rear end of each vehicle is shown in Fig. 10. The pressure distributions for variants 1 and 2 are quite similar. The key difference is that the pressure on the underbody is lower in variant 1, generating higher downforce. Because of the boundary layer separation in variant 3, the pressure at the rear bumper is much lower compared to variant 1 and variant 2. This explains the increased drag. Moreover, the pressure on the upstream part of the diffuser in variant 3 is much larger than in the other variants, which contributes to this variant generating lift. Thanks to the battery box fairing, some of the pressure at the rear bumper is recovered, although not entirely. Variant 4 experiences less lift than variant 3, in part because a low-pressure region is generated on the upstream part of the diffuser (due to which the flow turns upwards).

The pressure distribution on the front part of the underbody of each vehicle is shown in Fig. 11 (note that the pressure range is different to that used in Fig. 10). The front lift experienced by variant 3 is caused by a large
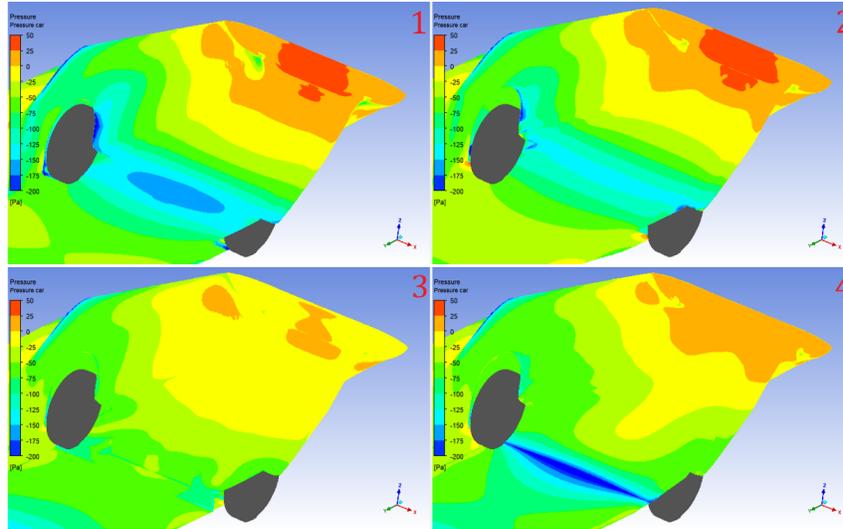
Figure 10: Pressure distribution towards the rear of the vehicles.

region of stagnation upstream from the battery box, which also contributes to increased drag. In variant 4, the fluid upstream from the battery box is gently turned downwards, without deceleration. Thanks to this, both the drag and the lift are reduced.
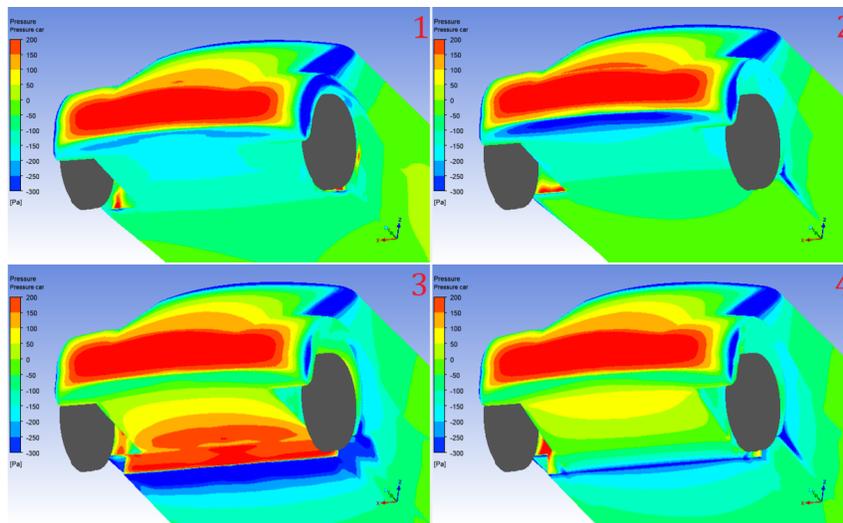

Figure 11: Pressure distribution at the front ends of the vehicles.

4 Summary

This study aimed to quantify the effect of an underbody battery box on the drag force on an electric vehicle. Computational fluid dynamics was used to examine the aerodynamic performance of four variants of the Eagle Two solar vehicle.

The downforce was observed to diminish by half when the ride height was increased from 12 cm to 22 cm, while the drag force increased slightly. When an underbody battery box was installed under the vehicle, the drag force almost doubled. Moreover, this configuration generated significant lift. As a solution, a battery box fairing was designed and tested. The fairing reduced the increase in drag caused by the battery box almost by half and decreased the unwanted lift almost entirely.

The design of the fairing presented in this study is fairly uncomplicated and easy to fabricate. Further research could consider more intricate shapes. Future work should be focused on reducing the separation zone behind the rear wheels. This could involve designing an aerofoil-shaped rear wheel fairing, which is a popular solution among teams competing in the Bridgestone World Solar Challenge in the Challenger Class. However, such a fairing would require a complicated manufacturing process.

The results of this study could contribute to the design of more stable and aerodynamically efficient electric vehicles, by allowing the battery box to be installed under the vehicle while keeping the drag within a reasonable range.

References

[1] Where the Energy Goes: Electric Cars. US DOE, US EPA. https://www.fueleco nomy.gov/feg/atv-ev.shtml (accessed 20 March 2021).

[2] Simmonds N., Pitman J., Tsoutsanis P., Jenkins K., Gaylard A., Jansen W.: *Complete body aerodynamic study of three vehicles.* SAE Tech. Pap. (2017), 2017-01-1529.

[3] Ahmed S.R. Ramm G., Faltin G.: *Some salient features of the time-averaged ground vehicle wake.* SAE Transactions **93**(1984), 2, 840222–840402, 473–503.

[4] Buchheim R., Deutenbach K.-R., Lückoff H.-J.: *Necessity and premises for reducing the aerodynamic drag of future passenger cars.* SAE Transactions **90**(1981), 1, 810010–810234, 758–771.

[5] Cooper K.R., Bertenyi T., Dutil G. Syms, J. Sovran G.: *The aerodynamic performance of automotive underbody diffusers.* SAE Tech. Pap. (1998), 980030, 150–179.

[6] Potthoff J.: *The aerodynamic layout of UNICAR research vehicle.* In: Proc. Int. Symp. on Vehicle Aerodynamics, Wolfsburg, 1982.

[7] Katz J.: *Race Car Aerodynamics: Designing for Speed.* Bentley, 1995.

[8] Hucho W.: *Aerodynamics of Road Vehicles. From Fluid Mechanics to Vehicle Engineering.* Butterworth-Heinemann, 1987.

[9] Katz J.: *Automotive Aerodynamics.* Wiley, 2016.

[10] Shinde, Gopal, Aniruddha Joshi, Kishor Nikam.: *Numerical investigations of the drivAer car model using opensource CFD solver OpenFOAM.* Tata Consult. Serv., Pune, 2013.

[11] *DrivAer Model.* https://www.mw.tum.de/en/aer/research-groups/automotive/driv aer/ (accessed 15 Apr. 2021).

[12] Jakirlic S., Kutej L., Hanssmann D., Basara B., Tropea C.: *Eddy-resolving simulations of the notchback 'DrivAer' model: Influence of underbody geometry and wheels rotation on aerodynamic behaviour.* SAE Tech. Pap. (2016), 2016-01-1602.

[13] abois M., Lakehal D.: *Very-large eddy simulation (V-LES) of the flow across a tube bundle.* Nucl. Eng. Des. **241**(2011), 6, 2075–2085.

[14] Heft A.: *Aerodynamic investigation of the cooling requirements of electric vehicles.* PhD thesis, Technische Universität München, Munich 2014.

[15] Heft A.I., Indinger T. Adams N.A.: *Introduction of a new realistic generic car model for aerodynamic investigations.* SAE Tech. Pap. (2012), 2012-01-0168.

[16] Janssen L.J., Hucho W.H.: The effect of various parameters on the aerodynamic drag of passenger cars. In: Advances in Road Vehicle Aerodynamics (H.S. Stevens, Ed.), 1973. 223-254.

[17] Wright P.G.: *The influence of aerodynamics on the design of Formula One racing cars.* Int. J. Vehicle Des. **3**(1982), 4, 383–397.

[18] Eagle Two. http://lodzsolarteam.p.lodz.pl/index.php/eagle-two/ (accessed 3 May 2021).

[19] Lanfrit M.: *Best Practice Guidelines for Handling Automotive External Aerodynamics with Fluent.* Fluent Deutschland, Darmstadt 2005.

[20] *Ansys Fluent Mosaic – new mesh generation technology incorporating hexahedral and polyhedral elements.* Symkom, Łódź 2019. https://symkom.pl/ansys-fluent-mosaic/ (accessed 16 March 2021).

[21] Ansys: *Ansys Fluent User's Guide.* 2013.

[22] Schlichting H.: *Boundary-Layer Theory.* McGraw Hill, 1979.

[23] Miao L., Mack S., Indinger T.: *Experimental and numerical investigation of automotive aerodynamics using DrivAer model.* In: Proc. ASME 2015 Int. Design Engineering Technical Conferences and Computers and Information in Engineering Conf., Boston, Aug. 2–5, 2015. V003T01A039. ASME.

[24] Heft A.I., Indinger T., Adams N.A.: *Experimental and numerical investigation of the DrivAer model.* In: Proc. Fluids Engineering Division Summer Meeting, Rio Grande, July 8–12, 2012, FEDSM2012-72272, 41–51. ASME.

[25] Heft A.I., Indinger T., Adams N.: *Investigation of unsteady flow structures in the wake of a realistic generic car model.* In: Proc. 29th AIAA Applied Aerodynamics Conf., June 2011, 3669.

[26] Ashton N., West A., Lardeau S., Revell A.: *Assessment of RANS and DES methods for realistic automotive models.* Comput. Fluids **128**(2016), 1–15.

[27] Guilmineau E., Deng G., Leroyer A., Queutey P., Wackers J., Visonneau M. (2016, June): *Assessment of RANS and DES methods for the Ahmed body.* In: Proc. ECCOMAS Cong. 2016 VII Eur. Cong. on Computational Methods in Applied Sciences and Engineering (M. Papadrakakis, V. Papadopoulos, G. Stefanou, V. Plevris, Eds.), Crete Island, 5-10 June 2016.

[28] Menter F.R.: *Zonal two equation $k - \omega$ turbulence models for aerodynamic flows.* In: Proc. 23rd Fluid Dynamics, Plasmadynamics, and Lasers Conf., Orlando, 6–9 July 1993, AIAA-93-2906.

[29] Ansys Inc.: Ansys Fluent 12.0 Theory Guide, 2009.

[30] Menter F.R.: *Two-equation eddy-viscosity turbulence models for engineering applications. AIAA J* **32**(1994), 8, 1598–1605.

[31] Sobczak K.: *Numerical investigations of an influence of the aspect ratio on the Savonius rotor performance.* J. Phys. Conf. Ser. **1101**(2018), 1, 012034.

[32] Huang P.G., Bardina J., Coakley T.: *Turbulence modeling validation, testing, and development.* NASA Tech. Memorand. (1997), 110446, 147.

[33] Pawłucki M., Kryś M.: *CFD for Engineers.* Helion, Gliwice 2020.